photonics

MDPI

Article

High-Performance Fiber Optic Gyroscope Based on a Silicon Photonic Integrated Circuit

Xinran Zhao [1], Yuefeng Shen [1], Yi Zhang [2], Ziqiang Zhao [2], Cui Liang [1], Yilan Zhou [1] and Tengchao Huang [1,3,*]

[1] College of Optical Science and Engineering, Zhejiang University, Hangzhou 310027, China; xinranwm@zju.edu.cn (X.Z.); 12330002@zju.edu.cn (Y.S.); cui_liang@zju.edu.cn (C.L.); naliyuohz@zju.edu.cn (Y.Z.)
[2] TROE Photonics, Hangzhou, Ltd., Hangzhou 311421, China; zhangyi@xight.ai (Y.Z.); zhaozq@xight.ai (Z.Z.)
[3] Jiaxing Research Institute, Zhejiang University, Jiaxing 314050, China
* Correspondence: huangtengchao@zju.edu.cn

Abstract

Fiber optic gyroscopes (FOGs) are core sensors in inertial navigation systems, and their miniaturization and integration are currently hot research topics. This work presents an FOG system driven by a silicon photonics integrated circuit (PIC). The PIC, based on a 90 nm silicon-on-insulator (SOI) process, integrates core components such as polarizers, 3 dB couplers, and phase modulators within a compact footprint of 3×0.45 mm^2. These components exhibit excellent performance over a wide spectral range and play a crucial role in high-performance FOG systems. Experimental results show that the proposed FOG system can definitively measure the small angular velocity of the Earth's rotation (± 7.5 °/h). Further Allan variance analysis reveals that the FOG system has an angular random walk (ARW) of 0.00358 °/h$^{1/2}$ and a bias instability (BIS) of 0.1185 °/h. These results demonstrate the application potential of silicon photonics-based FOG systems.

Keywords: optical gyroscope; photonic integrated circuit; silicon photonics

1. Introduction

Gyroscopes are the core of inertial systems and can accurately measure the angular velocity in inertial space. Therefore, gyroscopes are indispensable in fields such as aerospace, defense and automotive sectors where reliable inertial navigation is crucial [1]. Since their introduction in 1976 [2], fiber optic gyroscopes (FOGs) have made significant progress, achieving excellent sensitivity and stability [3]. Miniaturization of FOGs is a key direction for future development. Traditional fiber optic gyroscopes have successfully reduced the size of FOGs and achieved commercialization by using a lithium niobate ($LiNbO_3$) multifunctional integrated optical circuit (MIOC) that integrates polarization, beam splitting and phase modulation functions [4]. However, traditional $LiNbO_3$ waveguides (manufactured by proton exchange or titanium diffusion) have the problem of low contrast between the core and cladding refractive indices [5]. This weak optical confinement requires a large bending radius, resulting in a chip footprint on the order of centimeters, which limits the progress of further miniaturization.

In the field of fully integrated systems, Srinivasan et al. (2014) and Gundavarapu et al. (2018) from Bowers' group pioneered the use of low-loss silicon nitride (Si_3N_4) waveguides to demonstrate integrated coils with an angular random walk (ARW) of 19 °/hr/Hz$^{1/2}$ and a bias instability (BIS) of 58.7 °/h [6,7]. Similarly, Anello Photonics (2022) demonstrated a

Check for updates

Received: 16 May 2026
Revised: 6 June 2026
Accepted: 11 June 2026
Published: 13 June 2026

Copyright: © 2026 by the authors. Licensee MDPI, Basel, Switzerland. This article is an open access article distributed under the terms and conditions of the Creative Commons Attribution (CC BY) license.

silicon photonic optical gyroscope (SiPhOG) by replacing fiber optic coils with ultra-low-loss Si_3N_4 waveguide coils [8]. Despite these advances, there is still a significant gap in propagation loss between Si3N4 waveguides and optical fibers, which limits the effective coil length and, consequently, the final sensitivity of on-chip coil solutions.

In order to overcome the loss limitation of waveguide coils and make full use of photonic integration, a hybrid approach has gradually gained attention, which combines high-performance photonic transceiver chips with traditional low-loss fiber coils. Tran et al. (2017) demonstrated a heterogeneous III-V/Si driver chip with a size reduced to 4.5 mm^2 [9]. Subsequently, efforts from industry and academia have further improved this architecture: KVH Industries (2019) realized a tactical ARW with 0.59 $^\circ/h/Hz^{1/2}$ using a high polarization-maintaining waveguide [10]; Shang et al. (2022) proposed a novel FOG based on an integrated optical chip with an overall size of 30 × 30 × 30 mm^3 [11]; Wang et al. (2023) developed a silicon-based MIOC for tactical sensing [12]; Lu et al. (2024) reported a high-performance Si-SiN transceiver with a BIS of 0.003 $^\circ/h$ [13]. Recently, Li et al. (2025) achieved a BIS as low as 0.022 $^\circ/h$ using a thin-film lithium niobate (TFLN) platform [14]. Shang et al. proposed a three-axis interferometric fiber optic gyroscope based on a silica integrated optical chip, achieving a highly compact size of 50 × 50 × 30 mm while main-taining a tactical-grade bias stability of better than 0.5 $^\circ/h$ [15]. Sun et al. developed a passive photonic integrated chip based on an ultra-low-loss silicon nitride platform and applied it to an interferometric fiber optic gyroscope, effectively replacing traditional discrete optical components to achieve miniaturization while reaching an ultra-low bias instability of 0.009 $^\circ/h$ [16].

This paper presents an FOG system driven by a silicon photonic integrated circuit (PIC). The PIC is fabricated using a mature 90 nm SOI process. The PIC integrates core components such as polarizers, 3 dB couplers, and phase modulators, with a footprint of only 3 × 0.45 mm^2. Experimental results demonstrate that these devices exhibit good performance over a wide spectral range. By constructing a complete FOG system, we can definitively measure the minute angular velocity of the Earth's rotation and measure key system-level parameters using Allan variance analysis. These results demonstrate the application potential of silicon photonics-based FOG systems.

2. Design of the PIC-Driven FOG System

The schematic diagram of the FOG is shown in Figure 1a. This design is based on the traditional fiber optic gyroscope. The PIC integrates edge couplers (ECs), polarizers, 3 dB couplers, and phase modulators. To suppress phase errors caused by parasitic Michelson interference, a 678 μm delay waveguide is connected after one of the phase modulators. The PIC is fabricated on a standard 90 nm SOI platform. The connecting waveguides between devices are 500 nm wide and 220 nm thick. Therefore, the PIC can operate under stable single-mode conditions, while the waveguides provide strong light confinement, enabling the implementation of low-loss bent waveguides with a radius of 5 μm. We achieved a more compact device layout, with the final PIC size being only 3 × 0.45 mm^2, as shown in Figure 1b.

The optical coupling and electrical interconnection scheme of the PIC is shown in Figure 1c. The PIC and external components (light source, photodetector, fiber coil) are connected via two fiber arrays. UHNA7 fiber is used in the fiber array, with polarization-maintaining fiber fused to its tail to accommodate the external components. UHNA7 fiber has a small mode field diameter of about 3.2 μm and single-mode characteristics, which provides better matching with the edge coupler on the PIC [17,18]. The edge coupler adopts an adiabatic inverted conical structure (150 μm in length), with the narrower end (0.1 μm) aligned with the fiber to ensure mode matching with the edge coupler at the facet.

Test results show that the coupling between the edge coupler and UHNA7 has a flat loss (3.31 ± 0.14 dB) in the target wavelength range (1.53–1.57 μm). Mechanically, the PIC is securely mounted on a printed circuit board (PCB) and maintains the integrity of electrical signals through gold wire bonding between on-chip pads and the PCB.

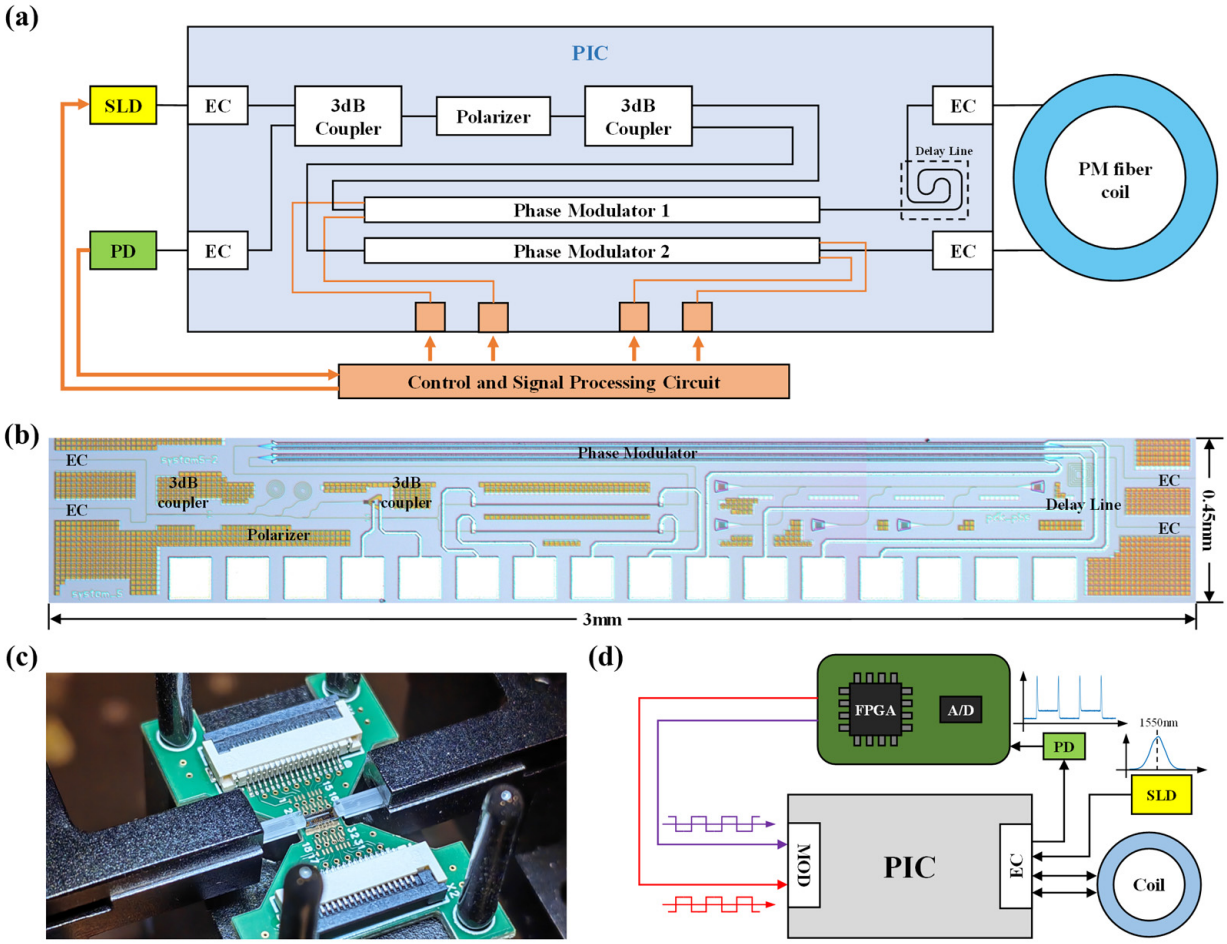

Figure 1. Overview of the FOG system assembly. (**a**) Schematic diagram showing the architecture of the FOG system. (**b**) Micrograph of the PIC. (**c**) Illustration of the interconnection between the fiber array and the PIC. (**d**) Characterization of the FOG system based on push–pull modulation. MOD: phase modulator. FPGA: Field Programmable Gate Array.

The connection between the PIC and external components in the FOG system is shown in Figure 1d. The light source is a superluminescent diode (SLD) with a center wavelength of 1550 nm and a full width at half maximum (FWHM) of 30 nm. A broadband light source is crucial for suppressing phase errors caused by coherent back reflection. The polarization-maintaining (PM) fiber coil is 1.2 km long, with a total transmission loss of less than 0.5 dB. A high-sensitivity (0.85 A/W) InGaAs PIN photodetector (PD) is used to convert the Sagnac interference signal into a current signal.

2.1. Polarizer

Polarizers are indispensable in the FOG system, used to maintain the polarization state of propagating light and mitigate polarization-induced errors [19]. A three-waveguide polarization beam splitter (PBS) based on mode-selective coupling is used in the PIC, as shown in Figure 2a. The device works by coupling the input fundamental transverse magnetic mode (TM0) to the center waveguide (TM1) and then to the cross port, while

the fundamental transverse electric mode (TE0) propagates through the direct port with minimal loss [20,21].

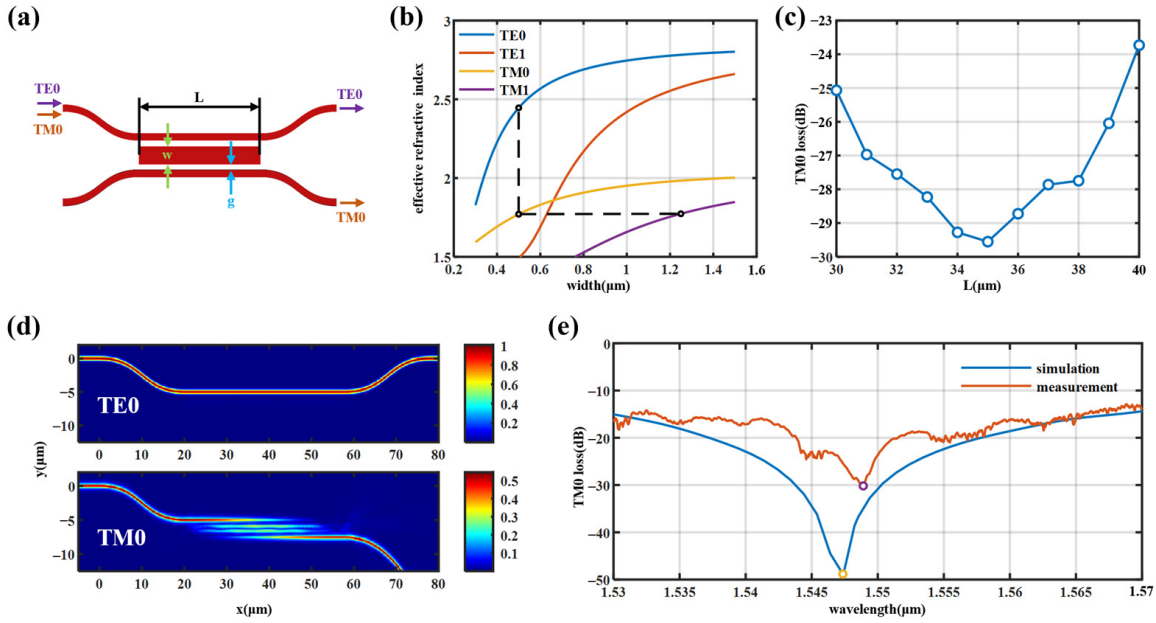

Figure 2. Design and characterization of the three-waveguide polarizer. (**a**) Schematic diagram illustrating the structure of the proposed three-waveguide polarizer. (**b**) Calculated effective refractive indices of the guided modes for a 0.22 μm thick silicon waveguide. (**c**) Dependence of the TM0 mode loss on the length of the bridging waveguide at a wavelength of 1.55 μm. (**d**) Simulated optical field propagation profiles for the TE0 and TM0 modes. (**e**) Comparison between the simulated and measured insertion losses for the TM0 mode.

The device's geometry was designed to achieve the optimal TM0 extinction ratio. With the input and output waveguide widths fixed at 0.5 μm, the width w of the intermediate bridging waveguide needed to be determined to satisfy the phase-matching condition. Figure 2b shows the effective refractive index versus waveguide width calculated using a finite difference eigenmode (FDE) solver (Ansys, Inc., Canonsburg, PA, USA). As shown in Figure 2b, the effective refractive index of the TM0 mode in the input waveguide is equal to that of the TM1 mode in a waveguide with a width of 1.25 μm. Therefore, the width w of the bridging waveguide was determined to be 1.25 μm. Subsequently, a waveguide gap (g) of 400 nm was chosen to ensure sufficient manufacturing tolerance. The maximum TM0 extinction ratio was obtained by scanning the length of the bridging waveguide using finite difference time domain (FDTD) simulation, as shown in Figure 2c. The electromagnetic field propagation shown in Figure 2d indicates that the TM0 mode is effectively coupled to the cross port and subsequently absorbed by the P-type doped waveguide, thus ensuring the propagation of a pure TE0 mode in the PIC.

Experimental results show that manufacturing tolerances cause discrepancies between simulated and measured performance. Nevertheless, the device exhibits stable performance within the operating wavelength range of 1.53–1.57 μm, achieving a TM0 mode extinction ratio better than −15 dB, as shown in Figure 2e. To meet the stringent polarization extinction ratio requirements of FOG systems, a three-stage cascaded polarization beam splitter (PBS) structure was employed, achieving a total polarization extinction ratio exceeding −45 dB.

2.2. 3 dB Coupler

3 dB couplers play a crucial role in FOG systems. They split the input optical signal into two paths of equal power and simultaneously combine the returning light, thus generating

an interference optical signal. Furthermore, they also facilitate the input of light from external SLD and the entry of interference signal into the detector. The characteristics of a 3 dB coupler include its splitting ratio and insertion loss. The splitting ratio is a key factor affecting the system's sensitivity and bias stability, as it directly determines the visibility of the interference signal.

The 3 dB coupler uses a trident waveguide structure consisting of three symmetrically arranged adiabatic tapered waveguides [22], as shown in Figure 3a. The tip width (w0) of each tapered waveguide linearly transitions to 0.5 μm over the same length (L). The gap between adjacent waveguides is 0.23 μm to ensure sufficient manufacturing tolerance while minimizing device size. The geometry of the 3 dB coupler is strictly symmetrical, which is crucial for ensuring a uniform splitting ratio. Electromagnetic field propagation is shown in Figure 3b. The fundamental mode input from the central tapered waveguide is adiabatically evolved and gradually propagated to the two lateral waveguides.

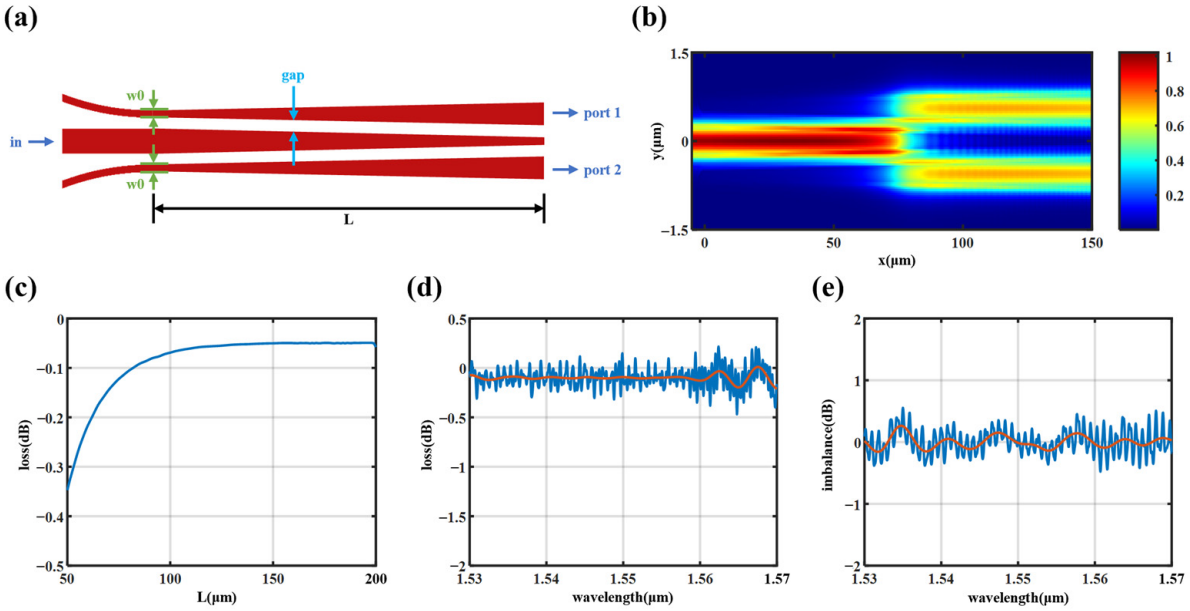

Figure 3. Design and characterization of the 3 dB coupler. (**a**) Schematic diagram of the proposed 3 dB coupler. (**b**) Simulated optical field propagation through the 3 dB coupler. (**c**) Coupling loss as a function of the coupler length. (**d**) Measured insertion loss. (**e**) Measured splitting imbalance at ports 1 and 2.

To reduce the insertion loss while controlling the size of the 3 dB coupler, we analyzed the relationship between coupler length and insertion loss using an eigenmode expansion (EME) solver (Ansys, Inc., Canonsburg, PA, USA). As shown in Figure 3c, the coupling loss converges and tends to stabilize when the tapered waveguide length exceeds 150 μm. Therefore, the length of the coupler was set to 150 μm. The feasibility of the 3 dB coupler was verified through testing. Figure 3d shows the insertion loss of the 3 dB coupler, which has a flat spectral response and an average loss of −0.09 dB, indicating that the coupler has broadband and low-loss characteristics. Furthermore, as shown in Figure 3e, the power splitting imbalance of the 3 dB coupler was controlled within ±0.5 dB.

2.3. Phase Modulator

In the realm of silicon photonics, the plasma dispersion effect is the main mechanism for realizing high-speed, high-efficiency optical phase modulators [23]. This effect modulates the phase by changing the effective refractive index of the waveguide by altering the concentration of free carriers (electrons and holes) within the waveguide [24]. Currently,

the main schemes for controlling carrier concentration include: (a) injecting carriers using a forward-biased PIN junction [25]; (b) depleting carriers using a reverse-biased PN junction [26]; and (c) carrier accumulation based on a metal-oxide-semiconductor (MOS) capacitor structure [27]. Although the modulation efficiency of PN junction modulators is lower than the other two, they remain the preferred scheme for FOG systems due to their excellent thermal stability and manufacturing process maturity.

Figure 4a shows the cross-section of a typical PN modulator. Under a reverse bias voltage, the applied electric field drives free carriers to move towards the P-type or N-type doped regions, resulting in a significant decrease in carrier concentration at the interface of the PN junction. As the reverse bias voltage increases, the depletion region widens. This process causes a change in the effective refractive index of the waveguide, while simultaneously reducing the loss of the waveguide caused by free carriers.

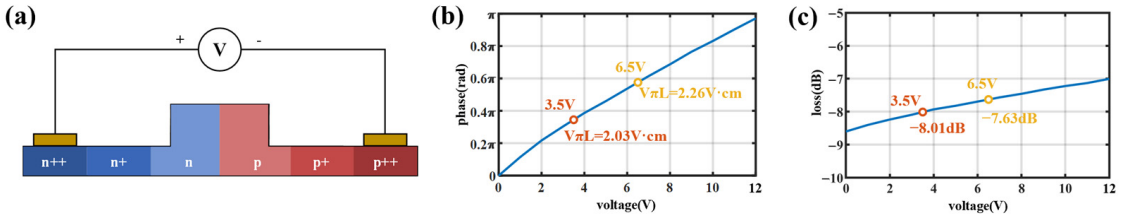

Figure 4. Design and characterization of the phase modulator. (**a**) Cross-sectional schematic of the PN phase modulator structure, where the number of "+" symbols indicates the carrier doping concentration levels. (**b**) Measured phase shift as a function of applied voltage. (**c**) Measured optical loss as a function of applied voltage.

We conducted performance tests using a Mach–Zehnder interferometer (MZI) structure comprising two 2 mm long phase modulators, and the results are shown in Figure 4b,c. The results indicate that the phase-voltage response of the PN modulator follows a nonlinear characteristic, with a half-wave voltage (Vπ) of 12.47 V. Simultaneously, the insertion loss changes by 0.38 dB when the applied reverse voltage is scanned from 3.5 V to 6.5 V. This leads to a power imbalance between the two arms of the interferometer. This not only reduces the visibility of the interference signal but also introduces non-reciprocal errors, thereby reducing the linearity of the scaling factor and the final bias stability of the gyroscope.

3. Performance of the PIC-Driven FOG System

The experiment on the FOG system was conducted using the structure shown in Figure 1d. The output power of the SLD was 6 dBm. Without the fiber coil connected, the output power from the PIC ports intended for the fiber coil was −13.6 dBm and −14.2 dBm, respectively. After connecting the fiber coil, the power received by the PD was −24.7 dBm.

The Field Programmable Gate Array (FPGA) serves as the control center of the FOG system. The modulation signal, a square-wave push–pull signal with a voltage range of 3.5 V to 6.5 V, is generated by the FPGA. This signal introduces a π/2 phase bias into the two arms of the interferometer, optimizing the gyroscope sensitivity. Furthermore, the FPGA acquires and processes the Sagnac interferometric signal at a rate of 2 kHz. Subsequently, this raw data is averaged, and the final angular velocity data is output at an update rate of 1 Hz.

To evaluate the sensitivity of the FOG system to low rotation rates, a static rotation test was conducted by horizontally mounting the fiber optic coil on an optical platform. The test location was at 30° North latitude, where the vertical component of the Earth's rotation rate was 7.5 °/h. After reversing the fiber optic coil by 180°, the detected Earth rotation

component changed from +7.5 °/h to −7.5 °/h. The raw data output from the FPGA was converted to angular velocity using the system's scaling factor, and the angular velocity bias was compensated. The angular velocity outputs before and after coil reversal are shown in Figure 5a, indicating that the system can clearly distinguish the Earth's rotation rate. Figure 5b shows the measurement results of the Earth's rotation rate over 1500 s. The data demonstrate that the FOG system can measure angular velocity with high stability under stable environmental temperature conditions.

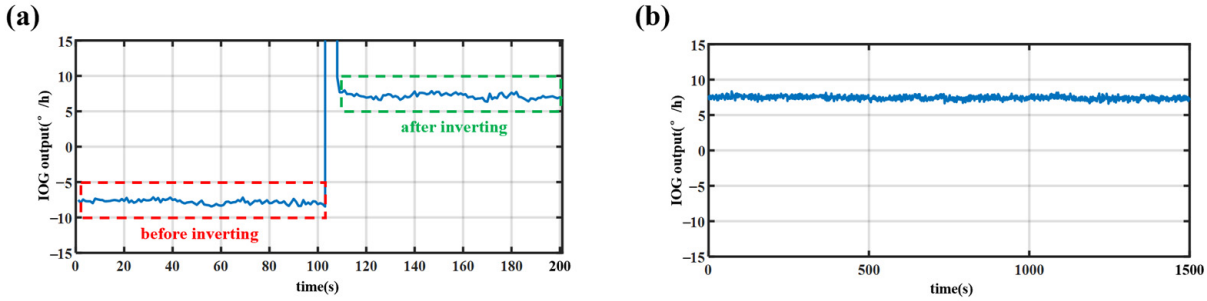

Figure 5. (**a**) FOG output angular velocity before and after inverting the horizontal fiber coil (corresponding to +7.5 °/h and −7.5 °/h). (**b**) FOG output angular velocity over a 1500 s duration with a horizontal fiber coil.

As shown in Figure 6, Allan variance analysis was used to further quantify the noise characteristics and long-term stability of the FOG system. The analysis results show that the ARW is 0.00358 °/$h^{1/2}$ and the BIS is 0.1185 °/h. These performance indicators show that the proposed FOG system successfully meets the requirements of a tactical-grade inertial sensor.

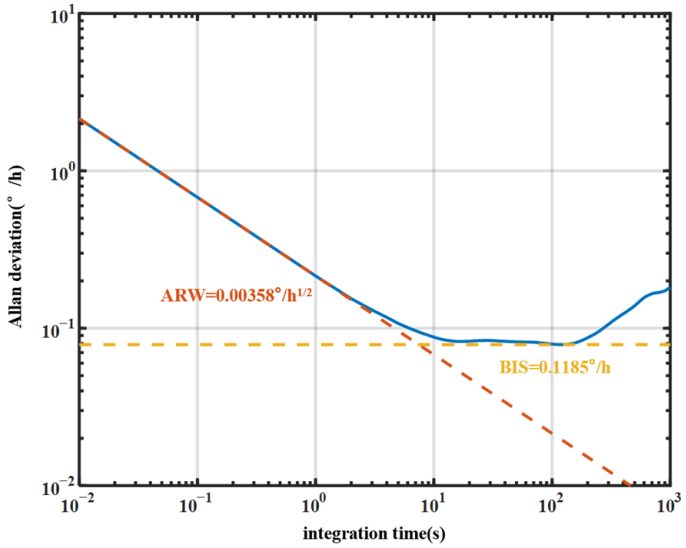

Figure 6. Allan deviation of the FOG system output results and performance indicators (ARW and BIS). The blue line indicates the Allan deviation.

To more clearly demonstrate the performance of the device, Table 1 provides a comprehensive comparison with recent works [12,28,29]. As shown in the table, the proposed device exhibits significant advantages in miniaturization and short-term noise performance (ARW), validating the effectiveness and practicality of the proposed PIC.

Table 1. Performance comparison with related works.

Reference	Platform	Footprint	Signal Detection Method	Coil (Length/Diameter)	Phase Modulator	ARW (°/h$^{1/2}$)	BIS (°/h)
[12] (2023)	SOI Active	4 × 1.2 mm^2	Open loop	1 km/10 cm	PN junction	0.097	0.105
[28] (2026)	SOI Active	5 × 2.5 mm^2	Open loop	1 km/10 cm	PN junction	0.015	0.08
[29] (2026)	SOI Active	0.4 mm^2 *	Open loop	1 km/10 cm	High-speed thermo-optic	0.04	0.91
This work	SOI Active	3 × 0.45 mm^2	Open loop	1.2 km/10 cm	PN junction	0.00358	0.1185

* The total footprint of the three-axis system is 1.2 mm^2.

4. Discussion

Despite the superior performance of the proposed PIC-driven FOG system, a significant performance gap exists between it and traditional FOGs, limiting its application in high-precision inertial navigation systems. Our analysis indicates that the main reasons limiting further performance improvements in the FOG system stem from inherent limitations of the SOI platform and insufficient chip packaging.

The 3 dB coupler acts as both beam splitter and combiner, and its beam splitting uniformity impacts system performance. The PN junction modulator based on the plasma dispersion effect exhibits varying insertion losses under different reverse bias voltages, resulting in different powers for the two returning beams. This power difference leads to reduced contrast and a decreased signal-to-noise ratio in the interference signal. Although we employed square-wave push–pull modulation to minimize modulator losses, this still introduces a 0.8 dBm power difference between the two beams.

Furthermore, the influence of higher-order modes in traditional fiber optic gyroscopes on the 3 dB coupler persists in our proposed FOG system. We have incorporated a double Y-junction structure consisting of two 3 dB couplers within the PIC. Light from the SLD, upon entering the first 3 dB coupler, excites higher-order modes, causing the second 3 dB coupler to exhibit non-uniform splitting ratio and initial phase deviation. This instability stems from the significant impact of environmental conditions such as temperature on the intensity and phase of higher-order modes, making the splitting ratio and phase difference in the second 3 dB coupler easily disturbed.

Imperfect coupling between the chip and the fiber also affects FOG performance due to reflections. As mentioned earlier, the broadband source in the FOG system and the delay waveguide in the PIC can eliminate phase errors caused by parasitic Michelson interference. However, these incoherent reflected lights still exist as background light in the PIC. This background light, superimposed on the Sagnac interference signal, increases the system's shot noise, thus hindering further resolution improvements in the FOG system.

During our evaluation, operating temperature significantly impacted the performance of the PIC-driven FOG due to silicon's high thermo-optic coefficient (1.86×10^{-4} K^{-1}), which leads to considerable variations in the waveguide's effective refractive index (neff). Figure 7a shows the simulated neff for a 500 nm × 220 nm waveguide with an effective coefficient of 1.98×10^{-4} K^{-1}. Among the on-chip components, the PN junction phase modulator exhibited the highest temperature sensitivity (compared to other passive components). Thermal fluctuations affect its depletion layer capacitance and carrier mobility, resulting in a simulated modulation efficiency (VπL) drift of 0.0004 V·cm/°C. This drift prevents the modulator from achieving a precise $\pi/2$ phase shift under a fixed applied voltage, introducing a modulation phase error of 3.14×10^{-4} rad/°C. These errors, combined with inherent parasitic amplitude modulation (PAM) and waveform asymmetry, distort the interference signal and cause significant bias drift. Although precise temperature control was not implemented to fully characterize metrics such as ARW and BIS, we evaluated this thermal effect through the system's output (Figure 7b). Within a temperature fluc-

tuation range of 1.5 °C, the measured angular velocity drifted by 35 °/h. Furthermore, simulations reveal that passive devices are also affected by thermal instability; for example, the insertion loss of the PBS for the TM0 mode varies with temperature by approximately 1 dB/°C. While this primarily reduces the polarization extinction ratio, rather than directly driving short-term bias drift as the modulator does, it exacerbates long-term polarization non-reciprocity, further reinforcing the necessity for stringent thermal management.

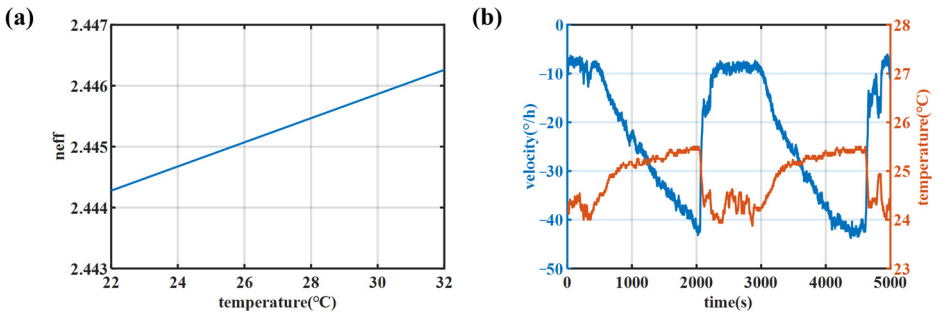

Figure 7. Impact of temperature on the FOG system. (**a**) Simulated effective refractive index (neff) variations in the silicon waveguide as a function of temperature. (**b**) Time-domain measurement of the FOG output angular velocity alongside ambient temperature fluctuations.

To further improve the overall performance of the PIC-driven FOG system, future research should focus on the following three aspects:

Structural optimization of on-chip core optoelectronic devices: Introducing an angled waveguide design at the edge coupler to reduce the interference of end-face back-reflections on the system's interferometric signal. A mode filter structure also should be implemented to effectively filter out higher-order modes, thereby reducing their crosstalk effects on the beam splitter's splitting ratio and the phase difference in the interference optical path. Additionally, the polarization extinction ratio of existing polarizers is highly sensitive to the effective refractive index of the waveguide and is highly susceptible to temperature fluctuations and fabrication tolerances. Future research should explore novel polarizer structures with higher robustness to thermal and geometrical variation.

High-stability optoelectronic packaging and active thermal management: The FR-4 PCB currently used in the system has a relatively large coefficient of thermal expansion (CTE). Under fluctuating thermal environments, thermal stress can induce micro-displacement between the fiber array and the PIC, leading to a degradation in coupling efficiency. Future research should employ substrate materials with closely matched CTEs and more mature optoelectronic co-packaging processes. To suppress thermal drift, a thermoelectric cooler (TEC) for active temperature control will be utilized alongside a precise temperature-dependent calibration and compensation algorithm.

Closed-loop signal processing algorithm design specific to silicon-based modulators: Due to significant differences in physical characteristics such as nonlinear phase response between silicon-based PN junction phase modulators and traditional lithium niobate modulators, the traditional FOG stepped-wave closed-loop feedback algorithm cannot be directly applied. Future research must investigate the response characteristics of PN junction modulators and develop novel digital closed-loop signal detection and feedback control algorithms to achieve high-precision angular velocity measurement over a large dynamic range.

5. Conclusions

In this paper, we have demonstrated a compact integrated optical gyroscope driven by a silicon photonic integrated circuit (PIC). The PIC is fabricated using a mature 90 nm SOI

process. High-PER polarizers, 3 dB couplers, and phase modulators are integrated onto a millimeter-scale chip. By employing a low-loss fiber coupling scheme, the system achieves robust stability and high sensitivity, capable of detecting rotational speeds comparable to the Earth's rotation rate. Experimental measurements show an ARW of 0.00358 °/$h^{1/2}$ and a BIS of 0.1185 °/h, which are excellent performances among current silicon-based integrated optical gyroscope implementations. Currently, the system's performance is limited by asymmetric modulator losses, higher-order mode crosstalk, back-reflections, and silicon's high thermal sensitivity. Future improvements will focus on optimizing on-chip structures to suppress optical noise, implementing advanced packaging with active thermal control, and developing customized closed-loop algorithms tailored for silicon modulators to achieve high-precision navigation.

Author Contributions: Conceptualization, X.Z. and Y.S.; methodology, X.Z.; software, X.Z.; validation, X.Z., Y.S. and Y.Z. (Yi Zhang); formal analysis, X.Z.; investigation, X.Z.; resources, Z.Z., C.L. and T.H.; data curation, X.Z. and Z.Z.; writing—original draft preparation, X.Z.; writing—review and editing, X.Z., Y.Z. (Yi Zhang) and Z.Z.; visualization, X.Z. and Y.S.; supervision, C.L. and Y.Z. (Yilan Zhou); project administration, C.L. and T.H.; funding acquisition, T.H. All authors have read and agreed to the published version of the manuscript.

Funding: This research was funded in part by "Pioneer" and "Leading Goose" Research and Development Program of Zhejiang through Zhejiang University, grant number 2024C01131; and in part by Key Research and Development Program of Jiaxing through Jiaxing Research Institute, Zhejiang University, grant number 2024BZ20017.

Institutional Review Board Statement: Not applicable.

Informed Consent Statement: Not applicable.

Data Availability Statement: Data is contained within the article.

Conflicts of Interest: Author Yi Zhang and Ziqiang Zhao were employed by the company TROE Photonics, Hangzhou, Ltd. The remaining authors declare that the research was conducted in the absence of any commercial or financial relationships that could be construed as a potential conflict of interest.

References

1. Lefèvre, H.C. The fiber-optic gyroscope, a century after Sagnac's experiment: The ultimate rotation-sensing technology? *Comptes Rendus Phys.* **2014**, *15*, 851–858. [CrossRef]
2. Vali, V.; Shorthill, R.W. Fiber ring interferometer. *Appl. Opt.* **1976**, *15*, 1099–1100. [CrossRef] [PubMed]
3. Passaro, V.M.N.; Cuccovillo, A.; Vaiani, L.; De Carlo, M.; Campanella, C.E. Gyroscope Technology and Applications: A Review in the Industrial Perspective. *Sensors* **2017**, *17*, 2284. [CrossRef] [PubMed]
4. Wooten, E.L.; Kissa, K.M.; Yi-Yan, A.; Murphy, E.J.; Lafaw, D.A.; Hallemeier, P.F.; Maack, D.; Attanasio, D.V.; Fritz, D.J.; McBrien, G.J.; et al. A review of lithium niobate modulators for fiber-optic communications systems. *IEEE J. Sel. Top. Quantum Electron.* **2000**, *6*, 69–82. [CrossRef]
5. Schmidt, R.V.; Kaminow, I.P. Metal-diffused optical waveguides in LiNbO3. *Appl. Phys. Lett.* **1974**, *25*, 458–460. [CrossRef]
6. Srinivasan, S.; Moreira, R.; Blumenthal, D.; Bowers, J.E. Design of integrated hybrid silicon waveguide optical gyroscope. *Opt. Express* **2014**, *22*, 24988–24993. [CrossRef]
7. Gundavarapu, S.; Belt, M.; Huffman, T.A.; Tran, M.A.; Komljenovic, T.; Bowers, J.E.; Blumenthal, D.J. Interferometric Optical Gyroscope Based on an Integrated Si3N4 Low-Loss Waveguide Coil. *J. Light. Technol.* **2018**, *36*, 1185–1191. [CrossRef]
8. Mike, H. Planar silicon nitride waveguide and silicon photonics integrated circuit for commercial optical gyroscope. In *Fiber Optic Sensors and Applications XVIII; Proceedings Volume PC12105*; Lieberman, R.A., Sanders, G.A., Scheel, I.U., Eds.; SPIE: Bellingham, WA, USA, 2022.
9. Tran, M.A.; Komljenovic, T.; Hulme, J.C.; Kennedy, M.J.; Blumenthal, D.J.; Bowers, J.E. Integrated optical driver for interferometric optical gyroscopes. *Opt. Express* **2017**, *25*, 3826–3840. [CrossRef]

10. Wang, L.; Halstead, D.R.; Monte, T.D.; Khan, J.A.; Brunner, J.; van Heyningen, M.A.K. Low-cost, High-end Tactical-grade Fiber Optic Gyroscope Based on Photonic Integrated Circuit. In Proceedings of the 2019 IEEE International Symposium on Inertial Sensors and Systems (INERTIAL), Naples, FL, USA, 1–5 April 2019; pp. 1–2.
11. Shang, K.; Lei, M.; Li, H.; Zhang, T.; Yu, X.; Xiang, Q.; Na, Y.; Zhang, L. Ultra-small interferometric fiber optic gyroscope with an integrated optical chip. *Chin. Opt. Lett.* **2022**, *20*, 040601. [CrossRef]
12. Wang, Y.C.; Lu, S.Y.; Yen, T.H.; Wei, C.C.; Chiu, Y.J.; Liu, R.Y.; Hung, Y.J. Silicon Photonics Multi-Function Integrated Optical Circuit for Miniaturized Fiber Optic Gyroscope. *J. Light. Technol.* **2023**, *41*, 6324–6332. [CrossRef]
13. Lu, Z.; Fu, H.; Sun, D.; Liu, H.; Jiao, H.; Fan, S.; Gao, S.; Li, T.; Wang, L.; Jin, L.; et al. Compact Si-SiN photonic fiber optic gyroscope transceiver for large volume manufacturing. *Photon. Res.* **2024**, *12*, 2912–2918. [CrossRef]
14. Li, X.; Pei, W.; Lu, Y.; Li, W.; Huang, A.; Jiao, H.; Feng, D.; Zhou, Z.; Feng, L. Thin-film lithium niobate multi-channel multifunctional photonic integrated chip for interferometric optical gyroscope. *Opt. Express* **2025**, *33*, 30669–30685. [CrossRef]
15. Shang, K.; Lei, M.; Li, H.; Feng, C.; Wei, S.; Zhao, H.; Yan, F. Tactical-Grade Three-Axis Interferometric Fiber-Optic Gyroscope with a Silica Integrated Optical Chip. *IEEE Sens. J.* **2025**, *25*, 10957–10963. [CrossRef]
16. Sun, D.; Jiao, H.; Li, H.; Wang, L.; Lu, Z.; Fan, S.; Liu, W.; Liu, H.; Ren, Z.; Yu, H.; et al. Interferometric Fiber Optic Gyro Based on High-Performance Passive Si3N4 Chip. *J. Light. Technol.* **2025**, *43*, 4740–4747. [CrossRef]
17. Shoji, T.; Tsuchizawa, T.; Watanabe, T.; Yamada, K.; Morita, H. Low loss mode size converter from 0.3 μm square Si wire waveguides to singlemode fibres. *Electron. Lett.* **2002**, *38*, 1669–1670. [CrossRef]
18. McNab, S.J.; Moll, N.; Vlasov, Y.A. Ultra-low loss photonic integrated circuit with membrane-type photonic crystal waveguides. *Opt. Express* **2003**, *11*, 2927–2939. [CrossRef]
19. Pavlath, G.A.; Shaw, H.J. Birefringence and polarization effects in fiber gyroscopes. *Appl. Opt.* **1982**, *21*, 1752–1757. [CrossRef]
20. Dai, D. Silicon Polarization Beam Splitter Based on an Asymmetrical Evanescent Coupling System with Three Optical Waveguides. *J. Light. Technol.* **2012**, *30*, 3281–3287. [CrossRef]
21. Kim, Y.; Lee, M.H.; Kim, Y.; Kim, K.H. High-extinction-ratio directional-coupler-type polarization beam splitter with a bridged silicon wire waveguide. *Opt. Lett.* **2018**, *43*, 3241–3244. [CrossRef]
22. Itoh, K.; Yuki, K.; Hayashi, Y.; Suzuki, J.; Amemiya, T.; Nishiyama, N.; Arai, S. Vertical trident coupler for 3D optical interconnection. In Proceedings of the 2016 IEEE 13th International Conference on Group IV Photonics (GFP), Shanghai, China, 24–26 August 2016; pp. 60–61.
23. Rahim, A.; Hermans, A.; Wohlfeil, B.; Petousi, D.; Kuyken, B.; Van Thourhout, D.; Baets, R.G. Taking silicon photonics modulators to a higher performance level: State-of-the-art and a review of new technologies. *Adv. Photonics* **2021**, *3*, 024003. [CrossRef]
24. Soref, R.; Bennett, B. Electrooptical effects in silicon. *IEEE J. Quantum Electron.* **1987**, *23*, 123–129. [CrossRef]
25. Baba, T.; Akiyama, S.; Imai, M.; Usuki, T. 25-Gb/s broadband silicon modulator with 0.31-V·cm VπL based on forward-biased PIN diodes embedded with passive equalizer. *Opt. Express* **2015**, *23*, 32950–32960. [CrossRef] [PubMed]
26. Thomson, D.J.; Gardes, F.Y.; Fedeli, J.M.; Zlatanovic, S.; Hu, Y.; Kuo, B.P.P.; Myslivets, E.; Alic, N.; Radic, S.; Mashanovich, G.Z.; et al. 50-Gb/s Silicon Optical Modulator. *IEEE Photonics Technol. Lett.* **2012**, *24*, 234–236. [CrossRef]
27. Sodagar, M.; Hosseinnia, A.H.; Isautier, P.; Moradinejad, H.; Ralph, S.; Eftekhar, A.A.; Adibi, A. Compact, 15 Gb/s electro-optic modulator through carrier accumulation in a hybrid Si/SiO_2/Si microdisk. *Opt. Express* **2015**, *23*, 28306–28315. [CrossRef]
28. Hung, Y.J.; Kuo, T.H.; Tsai, M.H.; Yang, S.T.; Chen, W.X. Silicon Photonics Multi-Function Integrated Optical Circuit with Hybrid III–V Photodiode for Miniaturized Fiber Optic Gyroscope Applications. *J. Light. Technol.* **2026**, *44*, 2613–2621. [CrossRef]
29. Chen, W.X.; Kuo, T.J.; Hung, Y.J. Thermally Stabilized Three-Axis Silicon Photonic Interferometric Fiber-Optic Gyroscope. In Proceedings of the 2026 IEEE Silicon Photonics Conference (SiPhotonics), Ottawa, ON, Canada, 13–15 April 2026; pp. 1–2.

Disclaimer/Publisher's Note: The statements, opinions and data contained in all publications are solely those of the individual author(s) and contributor(s) and not of MDPI and/or the editor(s). MDPI and/or the editor(s) disclaim responsibility for any injury to people or property resulting from any ideas, methods, instructions or products referred to in the content.